Low energy kaon photoproduction from nuclei*

A. Sibirtsev, W. Cassing, U. Mosel

Institut für Theoretische Physik, Universität Giessen
D-35392 Giessen, Germany

We study K^+-meson production in γA interaction at energies below the reaction threshold in free space. The Thomas-Fermi and spectral function approaches are used for the calculations of the production process. It is found that the measurement of the differential spectra may allow to reconstruct the production mechanism and to investigate the dispersion relations entering the production vertex. It is shown that the contribution from secondary pion induced reactions to the total kaon photoproduction is negligible for E_γ<1.2 GeV so that strangeness production at low energies is sensitive to the nuclear spectral function.

PACS: 13.40.-f; 13.60.Le; 13.75.Yz
Keywords: Electromagnetic processes; Meson production; Kaon-Baryon interactions

1. Introduction

The description of particle production in hadron-nucleus collision can be considered relatively to an energy scale given by the binding energy of the target [1]. The impulse approximation is an appropriate basis when the projectile energy is much higher than the binding energy and the target nucleons can be taken as free particles. However, at low energies the nuclear structure plays an essential role in the production process. When the bombarding energies are below the reaction threshold in free space the production process proceeds according to the energy available from the target. Now the reaction mechanism can no longer be considered as an interaction of the projectile with a quasi-free nucleon, but instead as an interaction with the whole nucleus, which might be approximated by the sum over the interactions with one nucleon (single scattering approximation), two nucleons (two nucleon current) and further many-body collisions [1–3].

In momentum space these many-body effects can be interpreted in terms of high momentum components of the nuclear wave function. As found in Ref. [4] these high momentum components of the nuclear wave function can be reasonably well described by short range two-nucleon correlations. In this sense the contribution from the high momentum components to particle production can be considered as a reaction mechanism due to the two-nucleon current.

Here we study the K^+-meson photoproduction from nuclei at energies below the $\gamma p \to K^+\Lambda$ reaction threshold in free space. This reaction has a set of advantages for an in-

*Supported by Forschungszentrum Jülich and DFG.

vestigation of the production mechanism. First, the elementary production amplitude is reasonably fixed by recent experimental results from ELSA [5]. Furthermore, the photon illuminates the whole nucleus, so the reaction also occurs deep inside the nuclear interior, while mesonic and baryonic projectiles confine the reaction to the nuclear periphery [6]. Moreover, K^+-mesons only weakly interact with the nuclear medium due to the strangeness conservation and thus the information about the production mechanism does not get distorted very much.

Historically [7], strangeness photoproduction from nuclei is considered as one of the optimal ways to study the formation of hypernuclei [6,8–10]. The hypernuclear production in γA reactions is part of the program at the Jefferson Laboratory [11]. Within the present work we demonstrate that the study of the K^+-meson production mechanism in photo-nuclear reactions [12] is an interesting subject, complementary to the hypernuclear experimental program, because it is sensitive to the nuclear spectral function. As indicated above, the optimal energies for studying the in-medium production mechanism are those below the reaction threshold in free space.

2. Elementary reaction

To describe the production process in nuclear matter we need the elementary $\gamma p \to K^+\Lambda$ reaction, which can be evaluated by the first order Feynman diagram. Following the pioneering studies by Gourdin and Dufour [13] or Thom [14] we include the Born terms in addition to low energy mesonic, nucleonic and hyperonic resonances, with properties fixed from the PDG [15] as listed in Table 1. We take into account the contribution from s, u and t channels, but neglect form factors at the interaction vertices. For the current status of the kaon photoproduction operator we refer the reader to Refs. [16,17].

Since we do not intend to extract the relevant coupling constants and resonance properties, but to construct simple parameterizations for the $\gamma p \to K^+\Lambda$ differential cross sections, we use the minimal set of parameters from Ref. [19].

The free parameters are fitted to the available data [5,18] on the differential $\gamma p \to K^+\Lambda$ cross section at photon energies from 0.926 GeV to 2.1 GeV. Polarization data are not included in the fit. The fitting procedure was performed by Minuit [20] and provides a reduced χ^2/N=3.88. The parameters G are listed in Table 1 where the notation for the coupling constants is that of Ref. [19]. Fig. 1 shows the experimental data [5,18] on the differential $\gamma p \to K^+\Lambda$ cross section in the cm-system for E_γ from 0.926 to 1.45 GeV whereas the solid lines indicate our parameterization.

3. K^+ distortion in nuclear matter

Because of the rather weak K^+-nucleon interaction the K^+-meson is considered as a promising probe for studying the production process in nuclear matter. Experimental data [15] on K^+p and K^+n cross sections are shown in Fig. 2a-b) together with the parameterizations from Ref. [21]. Note, that data are not available for the K^+n cross section at momenta below 800 MeV/c and the parameterization was constructed in line with the low energy limit from the Jülich model [22]. Within the experimental uncertainties the K^+N cross sections range from 9 to 18 mb at kaon momenta below 1 GeV/c. Therefore, at normal nuclear density the kaon mean-free-path is within the range of $\simeq$3.5$\div$7 fm,

Table 1
The particle properties from Ref. [15] and coupling constants G (in the notation of Ref. [19]) used in our model. The symbols V and T denote the vector and tensor coupling, respectively.

Particle	J^P	Mass (MeV)	Width (MeV)	G
Λ	$\frac{1}{2}^+$	1115.68		2.77±0.36
Σ	$\frac{1}{2}^+$	1192.64		9.23±0.44
K^*	1^-	891.66	50.8	-0.39±0.12^V
K^*				-0.001±0.18^T
K_1	1^+	1273	87	1.01±0.05^V
K_1				3.55±0.16^T
S_{11}	$\frac{1}{2}^-$	1650	150	-0.417±0.010
P_{11}	$\frac{1}{2}^+$	1710	100	-0.962±0.065
S_{01}	$\frac{1}{2}^-$	1405	50	-0.488±0.15
S_{01}	$\frac{1}{2}^-$	1670	35	17.41±0.32
S_{01}	$\frac{1}{2}^-$	1800	300	0.07±0.33

comparable to a typical nuclear size. Because of the large mean-free-path it is expected that K^+-mesons should be only slightly distorted especially for light targets.

A measure for the final state interaction is provided by the distortion factor κ, calculated within the Glauber model as

$$\kappa = 1 - \frac{A_{eff}(\sigma_{KN})}{A_{eff}(\sigma_{KN}=0)}. \tag{1}$$

Here A_{eff} is the effective number of nucleons participating in the production and propagation of the kaon, which in case of photoproduction is given as [23–26]

$$A_{eff}(\sigma_{KN}) = \int_0^{+\infty} d\mathbf{b} \int_{-\infty}^{+\infty} dz\ \rho(\mathbf{b},z)\ \exp[-\sigma_{KN} \int_z^{\infty} d\xi\ \rho(\mathbf{b},\xi)], \tag{2}$$

with $\rho(\mathbf{r})$ denoting the single-particle density, that was taken of Fermi type with parameters from Ref. [27]. The density function is normalized such that $A_{eff}(\sigma_{KN}{=}0){=}A$.

Fig. 2c) shows the K^+ distortion factor κ as a function of the K^+N cross section for γC and γPb interactions. The dashed area in Fig. 2c) indicates the cross section σ_{KN} in vacuum for kaon momenta below 1 GeV/c. Even for the carbon target there is a roughly 20% probability for the K^+-meson to interact in the nuclear interior. For the Pb nucleus the K^+ distortion is quite substantial. Because of strangeness conservation there are no inelastic channels apart from the $K^+n{\rightarrow}K^0p$ charge exchange reaction leading to K^+ absorption. The low energy K^+N interaction is entirely due to elastic scattering such that the K^+ distortion factor provides the probability for K^+N elastic scattering in nuclear matter.

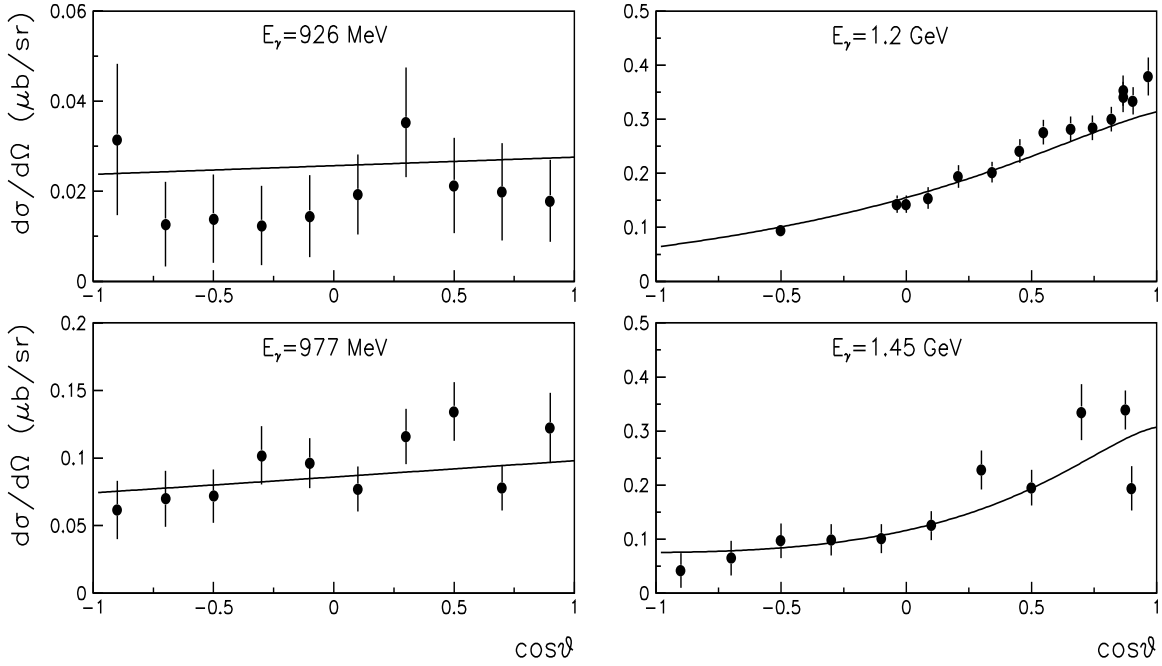

Figure 1. The differential $\gamma p \to K^+\Lambda$ cross sections in the cm-system at four different photon energies E_γ. The experimental data are taken from Refs. [5,18] while the lines show our fit.

Obviously, the $K^+N \to K^+N$ scattering distorts the information about the kaon production mechanism in nuclear matter and thus heavy nuclei are not suited for a relevant study. The elastic scattering populates the low energy part of the kaon spectrum, which can be also understood in terms of a thermalization process [28]. Thus, to reconstruct the production mechanism, light nuclear targets are an optimal choice and in the following we will use ^{12}C. Moreover, since the total K^+-meson flux is almost conserved (when neglecting the small absorption due to the $K^+n \to K^0p$ charge exchange) the A-dependence of the total K^+ production cross section can deviate from a linear scaling with A only due to the production process, which is not necessarily equivalent for light and heavy nuclei.

4. Dispersion relation in nuclei

The $\gamma p \to K^+\Lambda$ reaction threshold is given by energy conservation as

$$(m_K + m_\Lambda)^2 = (E_\gamma + E_N)^2 - (\mathbf{k}_\gamma + \mathbf{q}_N)^2 \,, \tag{3}$$

where in nuclear matter $q_N \neq 0$ and $E_N \neq m_N$. In principle, energy conservation provides the spectrum of nucleon momenta q_N and energies E_N available for $K^+\Lambda$ production, which depends on the photon energy. The dashed areas in Fig. 3 indicate the range of q_N and E_N that can energetically contribute to strangeness production at E_γ=700 and E_γ=900 MeV. The free dispersion relation $E_N = \sqrt{q_N^2 + m_N^2}$ is shown in Fig. 3 by the solid line.

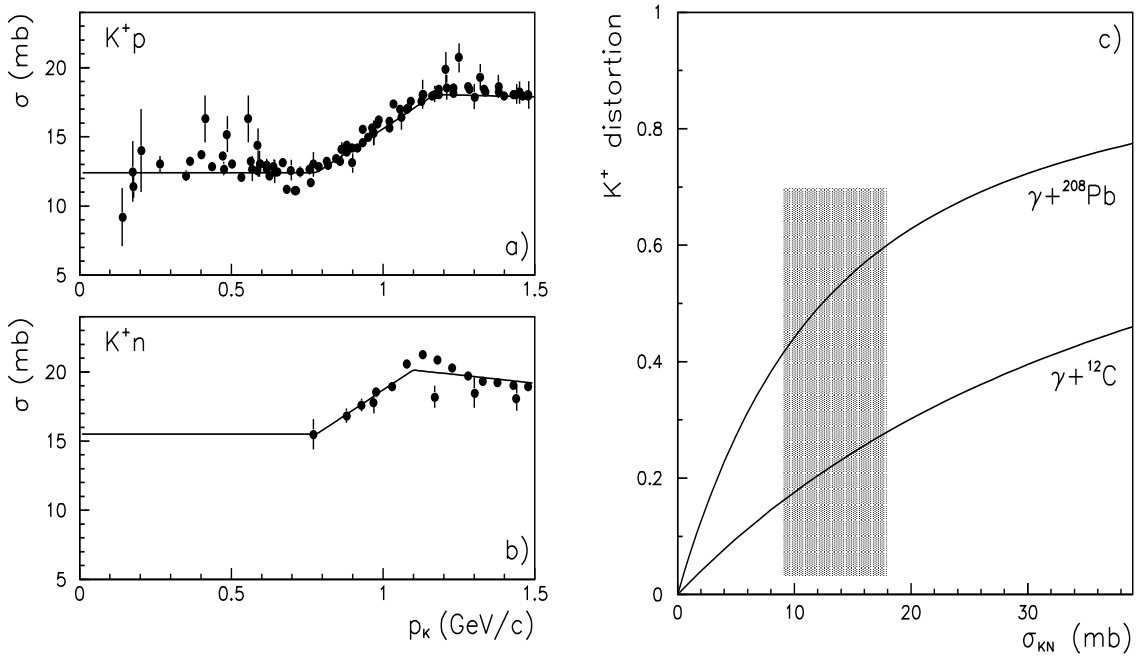

Figure 2. Total K^+p (a) and K^+n (b) cross sections as a function of the K^+-meson momentum from Ref. [15]. The solid lines in (a,b) show the parameterizations from Ref. [21]. (c) The K^+ distortion factor κ calculated in the Glauber model for γC and γPb as a function of the K^+-nucleon cross section. The dashed area indicates σ_{KN} in vacuum for kaon momenta below 1 GeV.

Using the free dispersion relation Fig. 3 illustrates that for $K^+\Lambda$ production at a photon energy of 700 MeV one needs nucleon momenta above $\simeq$260 MeV/c, which are only barely available in the Fermi sea. Note that the Fermi momentum for nuclear matter is $q_F\simeq$263 MeV/c, which is shown in Fig. 3 by an arrow. On the other hand, at E_γ=900 MeV the K^+-meson can be produced almost with $q_N\simeq$0, which reflects the fact that the $\gamma p\rightarrow K^+\Lambda$ reaction threshold lies at a photon energy of $\simeq$911 MeV in free space. The kinematical considerations shown in Fig. 3 motivate our present study of particle production at energies below the reaction threshold in vacuum. Indeed, it is clear that at photon energies below 900 MeV the $K^+\Lambda$ production becomes sensitive to nucleon momenta $q_N>q_F$ that may be attributed to the high momentum component of the nuclear wave function.

The situation is even exciting since in nuclear matter the free dispersion relation does not hold. There are different models [4,29–31] providing a relation between the nucleon momentum q_N and energy E_N in nuclei, but all of them correspond to an $E_N(q_N)$ spectrum below the free dispersion relation, i.e. below the solid line shown in Fig. 3.

Furthermore, the dispersion relations used for particle production in hadron-nucleus reactions cannot be uniquely fixed by theory; we thus suggest to study this important aspect of production dynamics by $\gamma A\rightarrow K^+\Lambda X$ reactions. To illustrate the sensitivity of observables to different dispersion relations we perform model estimates using two well-known approaches, i.e. the Thomas-Fermi approximation and the spectral function.

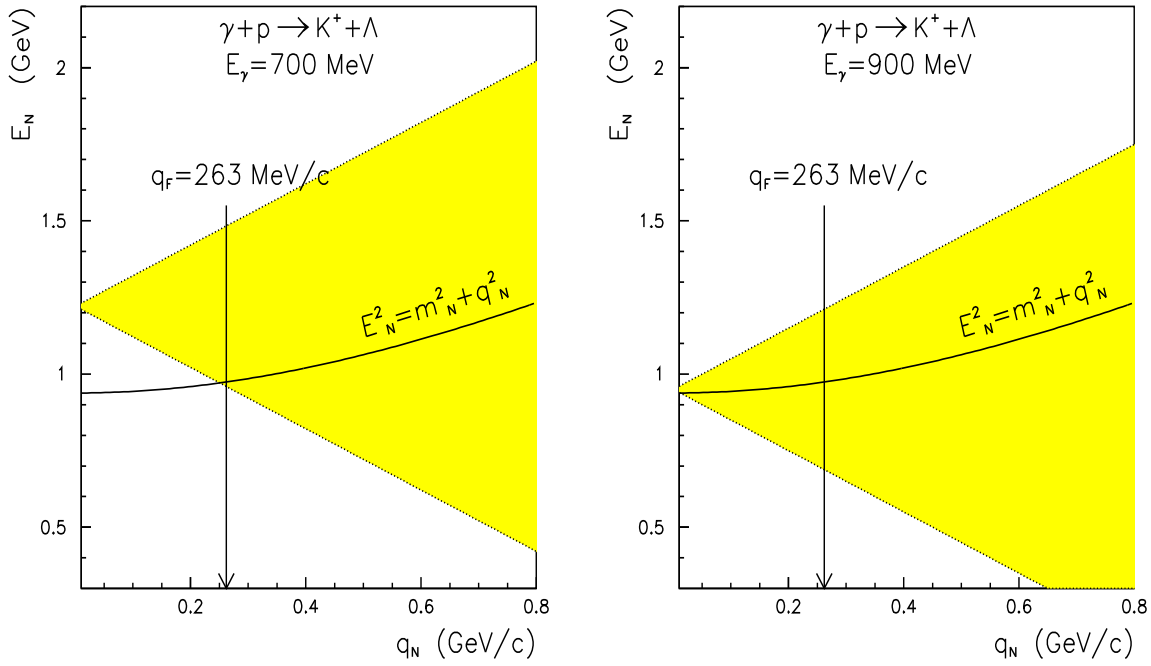

Figure 3. The energetically possible range (dashed area) of nucleon momenta q_N and energies E_N for the $\gamma p \rightarrow K^+\Lambda$ reaction at photon energies of 700 MeV and 900 MeV. The solid line indicates the dispersion relation in free space while the arrow shows the Fermi momentum for nuclear matter.

5. Thomas-Fermi approximation

In the noninteracting Fermi-gas model the occupation probability of states with momentum q_N is given by

$$\Phi(q_N) = \frac{3}{4\pi q_F^{3/2}} \Theta(q_F - |\mathbf{q}_N|), \tag{4}$$

where q_F is the Fermi momentum; for nuclear matter it is related to the average nuclear density ρ_0=0.16 fm^{-3} by

$$q_F = \left(\frac{3\pi^2\rho_0}{2}\right)^{1/3}. \tag{5}$$

The Fermi momenta for finite nuclei are given in Ref. [32]; for ^{12}C we have q_F=221 MeV/c. Within the local Tomas-Fermi approximation the total energy of the struck nucleon then is

$$E_N = \sqrt{q_N^2 + m_N^2} + U(q_N, \rho), \tag{6}$$

where m_N is the free nucleon mass and the nuclear potential U depends on the nucleon momentum q_N and density ρ. For the following calculations we adopt the potential given

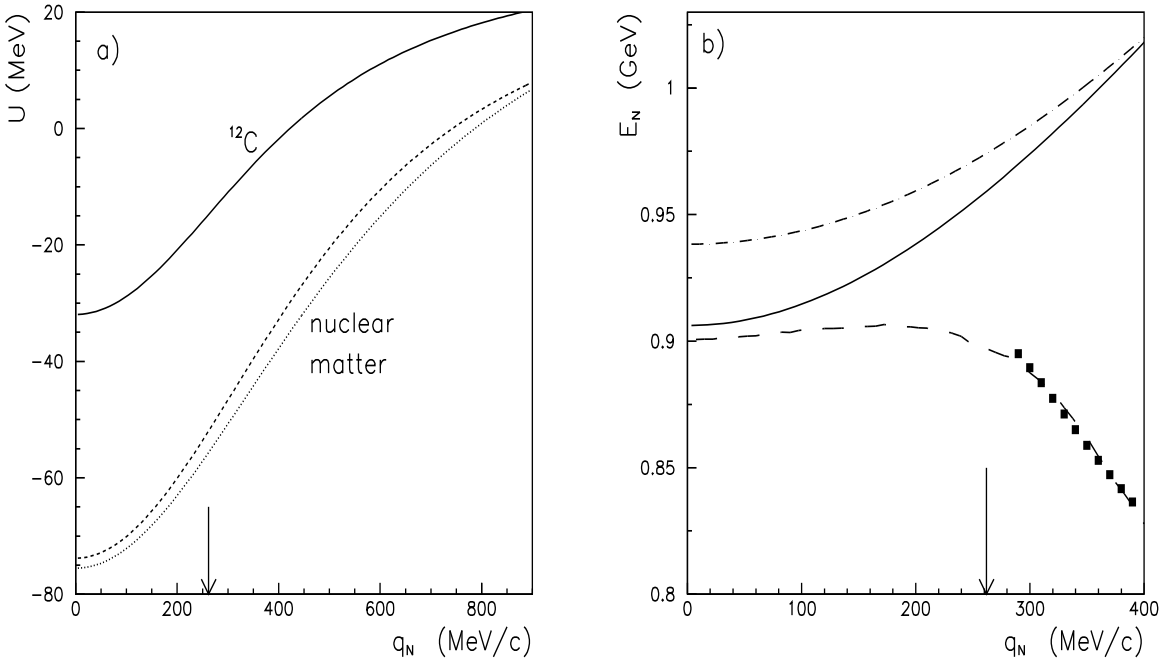

Figure 4. a) The single-nucleon potential at ρ=0.16 fm^{-3} as a function of the nucleon momentum q_N. The results for nuclear matter are shown by the dashed [34] and the dotted line [40]. The solid line shows the potential for ^{12}C calculated by Eq. (7) with q_F=221 MeV/c. The arrow indicates the Fermi momentum for nuclear matter. b) The dispersion relation $E_N(q_N)$ for ^{12}C. The solid line shows the relation (6) with the potential (7), the dash-dotted line is the free dispersion relation E_N=$\sqrt{q_N^2+m_N^2}$ while the long-dashed line shows the calculation with the spectral function. The squares display the result for the correlated part of the spectral function calculated by the model proposed in Ref. [4].

by Gale, Bertsch and Das Gupta [33] and Welke et al. [34] for cold nuclear matter as

$$U(q_N,\rho) = A_1\frac{\rho}{\rho_0} + B_1\left(\frac{\rho}{\rho_0}\right)^{1.24} + \frac{2\pi C_1\Lambda_1}{\rho_0}\left[\frac{q_F^2+\Lambda_1^2-q_N^2}{2q_N\Lambda_1}\times\ln\frac{(q_N+q_F)^2+\Lambda_1^2}{(q_N-q_F)^2+\Lambda_1^2}\right.$$
$$\left. +\frac{2q_F}{\Lambda_1} - 2\left(arctg\frac{q_N+q_F}{\Lambda_1} - arctg\frac{q_N-q_F}{\Lambda_1}\right)\right], \qquad (7)$$

where A_1=–110.44 MeV, B_1=140.9 MeV, C_1=-64.95 MeV and Λ_1=1.58q_F. The dashed line in Fig. 4a) shows the potential (7) for nuclear matter with q_F=262 MeV/c at ρ=ρ_0 as a function of the nucleon momentum. Note, that the mean field without momentum dependence provides $U\simeq$–53 MeV [35] for nuclear matter. The analysis of experimental scattering data using the Dirac equation [36–38] indicates that the potential becomes repulsive at nucleon energies E_{kin} above $\simeq$300 MeV.

The potential (7) for ^{12}C (using q_F=221 MeV/c) is shown by the solid line in Fig. 4a). In its ground state ^{12}C has two $s_{1/2}$ and $p_{3/2}$ single-particle levels [39] with excitation energies of $\simeq$–34 and –16 MeV, respectively. Indeed, Fig. 4a) indicates that the potential (7) approaches the lowest single-particle energy at low nucleon momenta.

Another optical potential was proposed by Wiringa [40] as

$$U(q_N,\rho) = A_2\frac{\rho}{\rho_0} + B_2\left(\frac{\rho}{\rho_0}\right)^2 + C_2\frac{\rho}{\rho_0}\left(1+[q_N/\Lambda_2]^2\right)^{-1}, \tag{8}$$

where A_2=15.52 MeV, B_2=24.93 MeV, C_2=-116 MeV and Λ_2=3.29−0.373(ρ/ρ_0) fm^{-1} [41]. The dashed line in Fig. 4a) shows the potential (8) for nuclear matter at density ρ=0.16 fm^{-3}, which at nucleon momenta below q_F (for density ρ_0) provides almost identical results as (7).

The dispersion relation for ^{12}C is given by Eq. (6) and shown in Fig. 4b) by the solid line while the dash-dotted line indicates the free dispersion relation E_N=$\sqrt{q_N^2+m_N^2}$. For low nucleon momenta q_N<100 MeV/c the Thomas-Fermi model with the Carbon potential is in rough agreement with the result from the spectral function approach of Ref. [31,42] shown in Fig. 4b) by the long-dashed line.

6. The spectral function

The short-range NN interactions induce correlations in the nuclear wave function, which deplete states below the Fermi sea and partially occupy the states above the Fermi level [29,43]. Thus the nuclear momentum distribution has a tail for momenta q_N>q_F. The dashed line in Fig. 5a) shows the momentum distribution $\Phi(q)$ from Ref. [4] due to the uncorrelated part of the spectral function, while the solid line indicates the total momentum distribution including the two-body correlations. Although the contribution from the high momentum component to the total function $\Phi(q)$ is small, its role can be important, since high nucleon momenta q_N might provide the large energies required for particle production below the reaction threshold in free space.

A nucleon in nuclear matter does not have a sharp energy E_N that is uniquely defined by its momentum q_N. The relation between the momentum and energy instead is given by the spectral function $S(q_N, E_N)$, which provides the joint probability of finding a nucleon with momentum q_N and energy E_N. The spectral function is generally given [30,31,44–47] in terms of the removal energy E_R, which is defined by energy conservation in the dissociation of nucleus A into nucleus B and a single nucleon as [32]

$$M_A = M_B + E_B^* + (m_N - E_R)\,, \tag{9}$$

where M_A and M_B are the masses of the nuclei A and B in their ground state and E_B^* is the excitation energy of the residual system B. Due to momentum conservation both, the residual system and nucleon, have the same modulus of the three-momentum q_N. In Eq. (9) the term in the brackets stands for the total nucleon energy and thus we have

$$E_N = m_N - E_R. \tag{10}$$

In the following calculations we use the spectral function for ^{12}C as given by Sick et al. [31,42], which is shown in Fig. 5b). Indeed, within the dispersion relation given by Fig. 5b) a certain nucleon momentum q_N is now related to the spectrum of the nucleon energy E_N. The contribution from $s_{1/2}$ and $p_{3/2}$ single-particle levels is indicated by the weak ridge at q<300 MeV/c, while the spectrum beyond the shell structure stems from

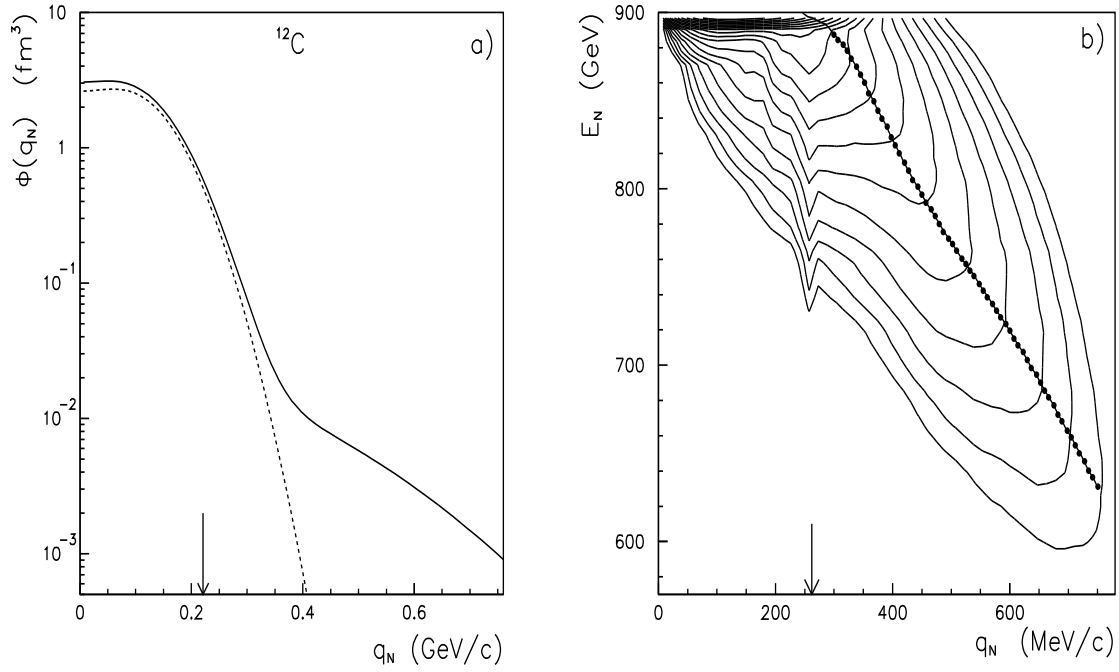

Figure 5. a) The nucleon momentum distribution $\Phi(q)$ for ^{12}C taken from Ref. [4]. The dashed line shows the uncorrelated part, while the solid line is the sum of the uncorrelated and correlated parts. The arrow indicates the Fermi momentum for ^{12}C from Ref. [32]. b) The dispersion relation given by the spectral function from Refs. [31,42]. The circles indicate the average nucleon energy calculated by Eq. (11).

the short-range and tensor correlations. It is important to note that on the average large momenta q_N>300 MeV/c are associated with small values of the nucleon energy E_N. The dependence of the average nucleon energy $< E_N >$ on the momentum q_N is given as

$$< E_N >= \frac{1}{\Phi(q_N)} \int_{E_{th}}^{\infty} E_N \; S(q_N, E_N) \; dE_N, \tag{11}$$

while the momentum distribution is related to the spectral function as

$$\Phi(q_N) = \int_{E_{th}}^{\infty} S(q_N, E_N) \; dE_N, \tag{12}$$

where E_{th} is the single nucleon removal threshold. The average nucleon energy is shown in Fig. 5b) by the dots and indicates that high nucleon momenta correspond to high removal energies. The dependence of $<E_N>$ on the momentum q_N can be compared to the dispersion relation given by the Thomas-Fermi model as shown in Fig. 4b). The result from the spectral function (solid line) is close to the Thomas-Fermi approach at q_N<100 MeV/c, but the two models differ substantially at larger momenta. Notice that even below the Fermi momentum q_F=221 MeV/c the difference is quite strong.

The squares in Fig. 4b) indicate the average nucleon energy $< E_N >$ resulting from the correlated part of the ^{12}C spectral function as calculated in the model proposed by Ciofi

degli Atti and Simula [4]. As can be seen, the agreement between the different models for the spectral function is very reasonable.

7. Results for K^+ production in γA reactions

The Lorentz-invariant differential cross section for K^+-meson production in γA reaction is given as [48]

$$E_K \frac{d^3\sigma_{\gamma A\to K\Lambda X}}{d^3p_K} = A_{eff}(\sigma_{KN}) \int d^3q_N \; dE_N \; S(q_N, E_N) \; \frac{Z}{A} \; E'_K \frac{d^3\sigma_{\gamma p\to K^+\Lambda}(\sqrt{s})}{d^3p'_K}, \tag{13}$$

where $\sqrt{s}$ is the invariant energy of the incident photon and the struck nucleon defined as

$$s = (E_\gamma + E_N)^2 - (\mathbf{k}_\gamma + \mathbf{q}_N)^2 \tag{14}$$

and the limits of integration in Eq. (13) are fixed by energy conservation as

$$m_K + m_\Lambda \leq \sqrt{s} \leq \sqrt{2E_\gamma M_A + M_A^2} - M_{A-1} \tag{15}$$

with M_A and M_{A-1} denoting the mass of the initial and final $A-1$ nuclei, respectively. Note, that the upper limit in (15) corresponds to the ground state of the residual $A-1$ nucleus and provides the maximal available energy $\sqrt{s}$ of the interaction vertex.

The primed indices in Eq. (13) denote the K^+-meson momentum and energy in the cms of the photon and the individual target nucleon, while $E'_K d^3\sigma/d^3p'_K$ is the Lorentz invariant elementary cross section for the $\gamma p \to K^+\Lambda$ reaction in free space as described in Sect. 2. The factor Z/A accounts for the fact that the reaction takes place only on the target protons.

The factor A_{eff} stands for the effective primary collision number as well as for the in-medium distortion of the K^+-meson when propagating through the nuclear target as described in Sect. 3. Note, that A_{eff}=A when neglecting the kaon distortion.

The total cross section for the $\gamma C\to K^+\Lambda X$ reaction is calculated with different models for $S(q_N, E_N)$ and shown in Fig. 6 as a function of the photon energy. The absolute reaction threshold given by the coherent production is indicated in Fig. 6 by an arrow. We observe that the result for the total cross section depends substantially on the model applied. At high energies E_γ>1.2 GeV both models roughly give the same total cross section. At $E_\gamma\simeq$800 MeV the difference between the calculations with the spectral function and the Thomas-Fermi approach amounts to a factor of about 6, which results from the different dispersion relations applied to the target nucleon. This can easily be understood by inspection of Fig. 4b).

One of the direct ways to extract the dispersion relation can be understood in terms of the four momentum squared Q_N^2 of the target nucleon. Within the Thomas-Fermi model it is given as

$$Q_N^2 \simeq (m_N + U)^2, \tag{16}$$

where we imply $q_N \ll m_N$. With the potential given by Eq. (7) one can estimate $Q_N^2 \simeq$ 0.8 GeV^2. Moreover, within the Thomas-Fermi approximation Q_N^2 is always positive and does not depend on the photon energy.

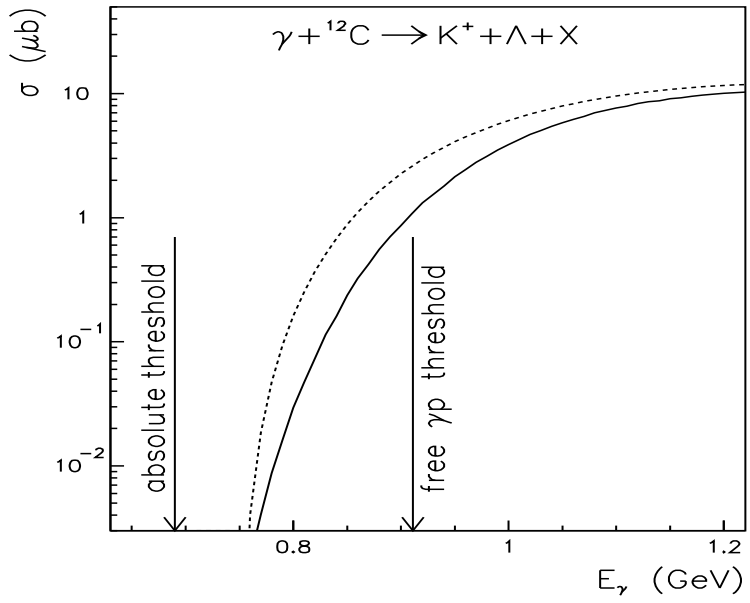

Figure 6. The $\gamma C \to K^+ \Lambda X$ total cross section as a function of the photon energy E_γ. The lines show calculations with the spectral function (solid) and Thomas-Fermi model (6) (dashed) while the arrows indicate the absolute γA and free γp reaction threshold.

Within the spectral function approach the quantity Q_N^2 is distributed as

$$\frac{d\Psi}{dQ_N^2} = \oint d^3q_N \, dE_N \, S(q_N, E_N) \tag{17}$$

where the integration is performed over the countour $Q^2 = E_N^2 - q_N^2$. The function (17) is shown in Fig. 7a). The negative part of the Q_N^2 spectrum corresponds to high nucleon momenta q_N and small energies E_N. In Fig. 7a) the arrow denoted by B shows the squared bare mass of the nucleon, while the arrow denoted by TF indicates the value for Q_N^2 as given by the Thomas-Fermi approximation (6). It is seen that the Q^2 distribution extends well below B.

It is clear that at photon energies above the reaction threshold in free space the total Q_N^2 spectrum, as given by the spectral function, is available for $K^+\Lambda$ production. Fig. 7b) shows the Q_N^2 spectra calculated for the $\gamma C \to K^+ \Lambda X$ reaction at E_γ=0.8, 1.0 and 1.2 GeV.

The Q_N^2 spectrum can be obtained experimentally from the four-momenta of the produced K^+-mesons and hyperons as

$$Q_N^2 = E_N^2 - q_N^2 = (E_K + E_\Lambda - E_\gamma)^2 - (\mathbf{p}_K + \mathbf{p}_\Lambda - \mathbf{k}_\gamma)^2 \tag{18}$$

Note, that relation (18) is similar to the experimental analysis for the reconstruction of the spectral function $S(E_N, q_N)$ in electron-nucleus scattering [32]. We also note, that the Q_N^2 spectra shown in Fig. 7b) might be substantially distorted due to the final state interaction of both the K^+-mesons and the Λ-hyperons. Similar problems also appear in $eA \to e'pX$ studies.

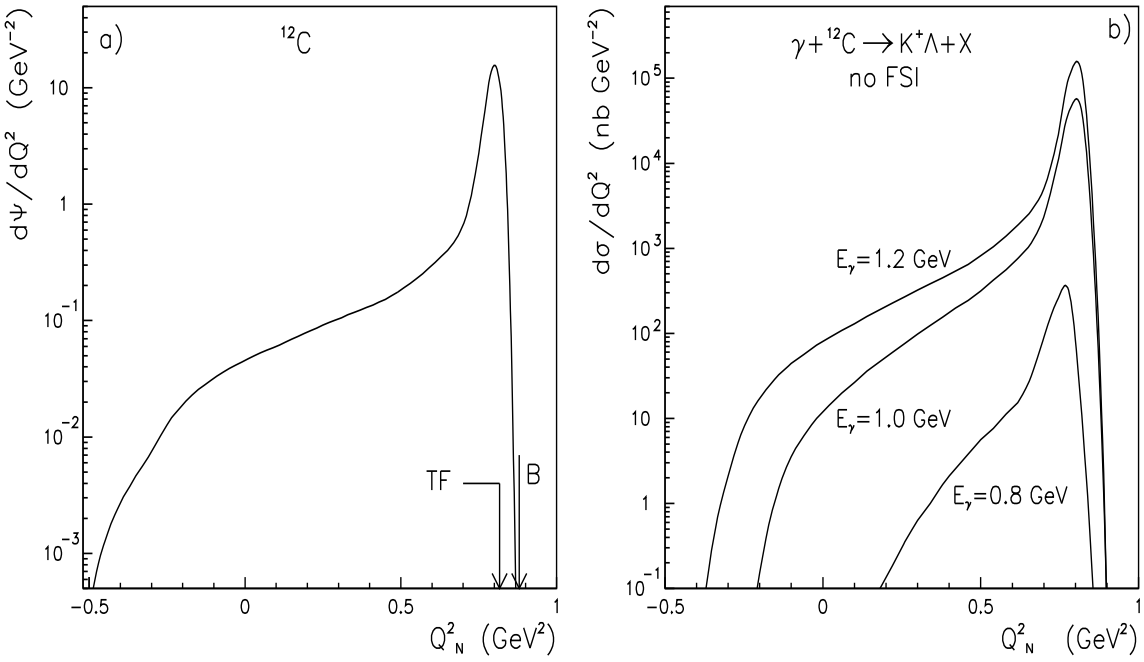

Figure 7. a) The Q_N^2 spectrum $d\Psi/dQ_N^2$ given by the spectral function for ^{12}C. The arrows denote the Thomas-Fermi limit (6) (TH) and the squared nucleon mass B. b) The differential Q_N^2 spectra calculated for the $\gamma C \rightarrow K^+\Lambda X$ reaction at different photon energies E_γ.

Another sensitive observable is the transverse momentum (p_t) spectrum of the produced kaons. In the elementary interaction between the photon and the target nucleon the transverse component of the total initial momentum is given by the nucleon momentum q_N, which is different in the Thomas-Fermi and the spectral function approximation. Due to momentum conservation the p_t distribution of the produced K^+-mesons reflects the transverse part of the q_N distribution.

The p_t spectrum for K^+-mesons from the $\gamma C \rightarrow K^+\Lambda X$ reaction at E_γ=800 MeV is calculated within the two models and shown in Fig. 8a). The solid histogram shows the calculations with the spectral function, the dashed one that obtained with the Thomas-Fermi approach. The results indicate that the absolute magnitudes of the differential cross sections from the two models are substantially different for p_t<170 MeV/c in line with the result shown in Fig. 6. The solid line in Fig. 8a) shows the calculations with the spectral function multiplied by a factor of 6 in order to account for the absolute difference in the total production cross section from the models. The shape of the p_t spectra from the two models differs at large p_t>170 MeV/c because in the Thomas-Fermi approximation the nucleon momenta q_N are limited to values below q_F.

Fig. 8b) shows the momentum spectrum of K^+-mesons from the $\gamma C \rightarrow K^+\Lambda X$ reaction at E_γ=800 MeV integrated over the laboratory angle $0<cos\theta<10^0$. Again we find a substantial difference between the calculations with the spectral function (solid histogram) and Thomas-Fermi approximation (dashed histogram) in the absolute value of the production cross section.

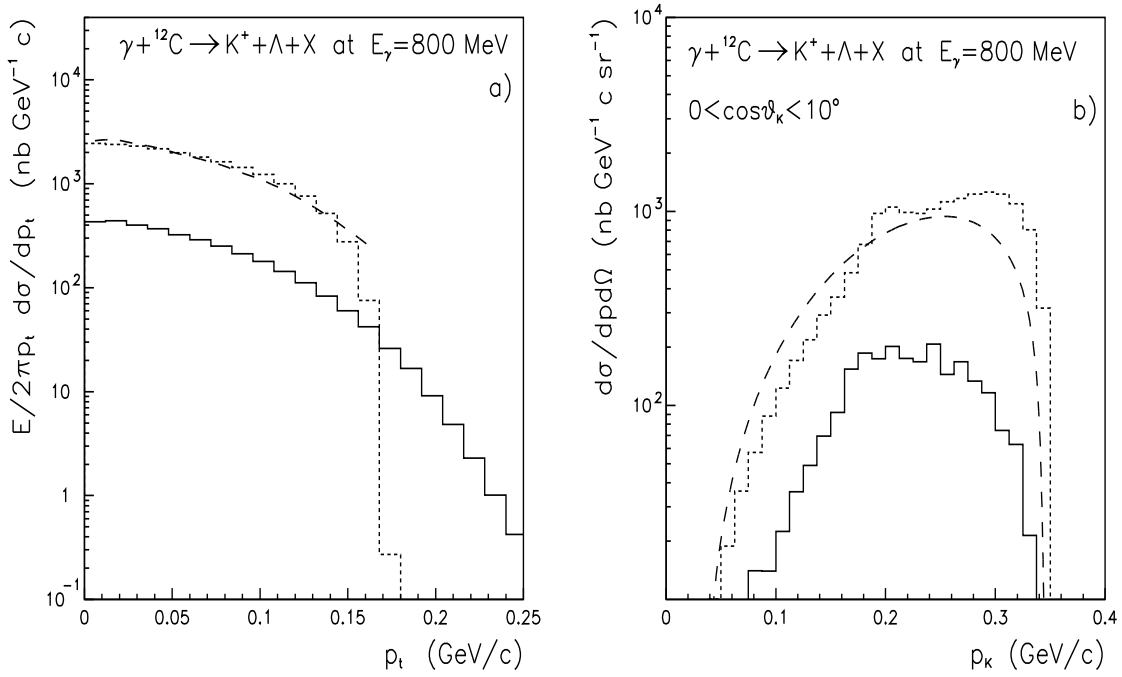

Figure 8. The transverse (a) and total momentum spectrum (b) at $0<cos\theta<10^0$ of K^+-mesons from the $\gamma C \to K^+\Lambda X$ reaction at a photon energy of 800 MeV. The histograms show the calculations with the spectral function (solid) and Thomas-Fermi model while the long-dashed line is the calculation with the spectral function multiplied by a factor of 6.

To compare the shapes of the momentum spectra we have renormalized the calculations with the spectral function and show this result in Fig. 8b) by the long-dashed line. Both models provide different shapes of the momentum spectrum. The calculations with the Thomas-Fermi model indicate a detectable enhancement at large K^+-meson momenta. A measurement of the K^+ spectra from $\gamma C \to K^+\Lambda X$ reaction at E_γ=800 MeV and at forward angles is thus sensitive to the dispersion relation.

8. Contribution from secondary processes

In principle, the $K^+\Lambda$ production in γA interactions can also proceed through a two-step process with an intermediate pion from the $\gamma N \to \pi N$ reaction followed by $\pi N \to K^+\Lambda$. The cross sections for K^+-meson production from the secondary pion induced reactions is calculated as [48–50]

$$E_K \frac{d^3\sigma_{\gamma A\to K\Lambda X}}{d^3p_K} = \int\limits_\Omega d^3q_N \; dE_N \frac{d^3p'_\pi}{E'_\pi} \; S(q_N, E_N) \; A_{eff}(\sigma_{\pi N}, \sigma_{KN}) \times \frac{1}{\sigma_{tot}} E''_K \frac{d^3\sigma_{\pi N\to K\Lambda}(\sqrt{s})}{d^3p''_M} \; E'_\pi \frac{d^3\sigma_{\gamma N\to \pi N}(\sqrt{s'})}{d^3p'_\pi}, \tag{19}$$

where the double prime indices denote the system of the intermediate pion and a target nucleon, while the single prime indices are those for the photon and the first target nucleon.

Moreover, $E_\pi d^3\sigma_{\gamma N\to\pi N}/d^3p_\pi$ stands for the π-meson differential production cross section, which is calculated in line with Eq. (13) assuming on-shell pions in the nuclear medium, while σ_{tot} is the total πN cross section.

In Eq. (19) the index Ω stands for the Pauli blocking of the final states from the $\gamma N\to\pi N$ reaction. Furthermore, the factor A_{eff} in Eq. (19) accounts for the effective primary collision number, pion interaction in the nuclear interior as well as for the in-medium distortion of the produced K^+-meson. It is calculated by an integration over the path of the produced π-mesons and final kaons as proposed in Ref. [25,26].

The elementary $\gamma N\to\pi N$ reaction is calculated in line with the results from the Virginia WI98K partial wave analysis [51]. Note, that three reaction channels: $\gamma p\to\pi^+ n$, $\gamma p\to\pi^0 p$ and $\gamma n\to\pi^0 n$ enter the two-step process calculations of $K^+\Lambda$ photoproduction.

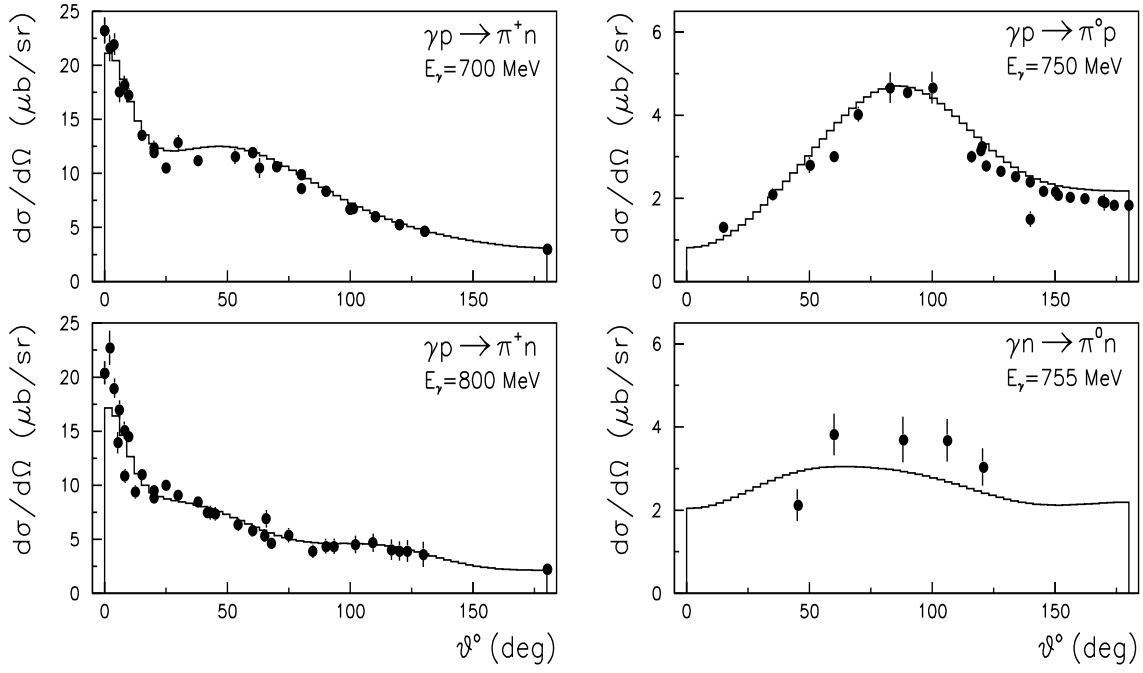

Figure 9. The differential cross sections for different channels of the $\gamma N\to\pi N$ reaction at several photon energies. The circles show the experimental data [18,52] while the histograms indicate our simulations based on the Virginia WI98K partial wave analysis [51].

Fig. 9 shows the experimental data [18,52] on the differential cross sections for various reaction channels at several photon energies E_γ in comparison with the simulation code. Since the WI98K partial wave solution describes the data up to E_γ=2 GeV, we believe to be accurate within this energy range. The cross sections for the $\pi^0 p\to K^+\Lambda$ and $\pi^+ n\to K^+\Lambda$ reactions are taken from the resonance model calculation of Tsushima et al. [53,54]. As shown in Ref. [53,54] the resonance model reproduces the data well up to $K^+\Lambda$ invariant masses of $\simeq$2 GeV.

Here we do not account for multi-pion production in γN reactions, which might enhance the contribution from the secondary processes. Since the π-meson spectra from multi-

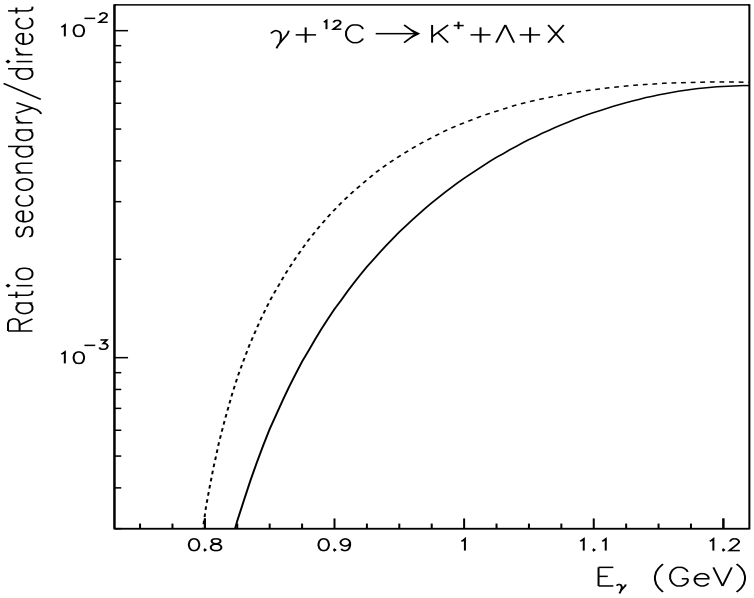

Figure 10. The ratio of the contribution to the $\gamma C \rightarrow K^+ \Lambda X$ reaction cross section from two-step to direct production process as a function of the photon energy E_γ. The dashed line shows the calculations within the Thomas-Fermi model (6) while the solid line gives the result of the spectral function approach.

pion production at $E_\gamma \leq 1$ GeV are soft [55] and have their main strengh essentially below the $\pi N \rightarrow K^+ \Lambda$ threshold, we consider our estimate for the contribution from secondary processes as a lower limit.

The dashed line in Fig. 10 shows the ratio of the $K^+\Lambda$ production cross section from secondary processes to the contribution from the direct production calculated within the Thomas-Fermi approximation. At $E_\gamma < 1.2$ GeV the contribution from the two-step reaction mechanism amounts to less than 1%. The solid line in Fig. 10 shows the calculations with the spectral function. We thus conclude that the contribution from the two-step process to the $\gamma C \rightarrow K^+ \Lambda X$ reaction is almost negligible at photon energies below 1.2 GeV.

In our study on subtreshold meson production from pA collisions [48] it was found that the contribution from secondary pion induced reactions dominates the direct production mechanism. This finding is different from our present result obtained for the γA reactions and needs further explanation.

Fig. 11a) shows the rate of the pion production in γp and pp interactions as a function of the projectile momentum. This rate is defined as a ratio of the π-meson production cross section to the total reaction cross section. Let us to consider the role of the secondary reaction mechanism at energies below the direct $\gamma p \rightarrow K^+ \Lambda$ and $pp \rightarrow K^+ \Lambda p$ production thresholds, which are indicated in the Fig. 11a) by the arrows. It is clear that near the direct production threshold the π-meson production rate is almost the same for the γ and p induced reaction. We thus conclude that the strength of the secondary process at a given projectile momentum is also almost the same for the photon and proton induced reactions on nuclei.

Fig. 11b) shows the rates of direct $K^+\Lambda$ production from γp and pp reactions as a function of the excess energy ϵ. Here ϵ is given as the difference between the invariant collision energy and the total mass of the final particle. Both the experimental data and our calculations indicate that the rate of the $\gamma p \rightarrow K^+\Lambda$ reaction is substantially (by about two orders of magnitude) larger than the $pp \rightarrow K^+\Lambda p$ rate at energies close to the threshold in free space. Thus the direct $K^+\Lambda$ production dominates in photon induced reactions on nuclei and the cross section is thus directly sensitive to the spectral function of the nucleon in the target nucleus.

This is an important finding indicating the advantage of the γA reactions in styding the production at energies below the reaction threshold on a free nucleon. An additional study is interesting in order to understand if the production of heavy mesons such as ρ, ω and ϕ show the same tendency. We also refer to Ref. [55], where a dominance of the direct production mechanism was found for subthreshold η-meson production in γA reactions.

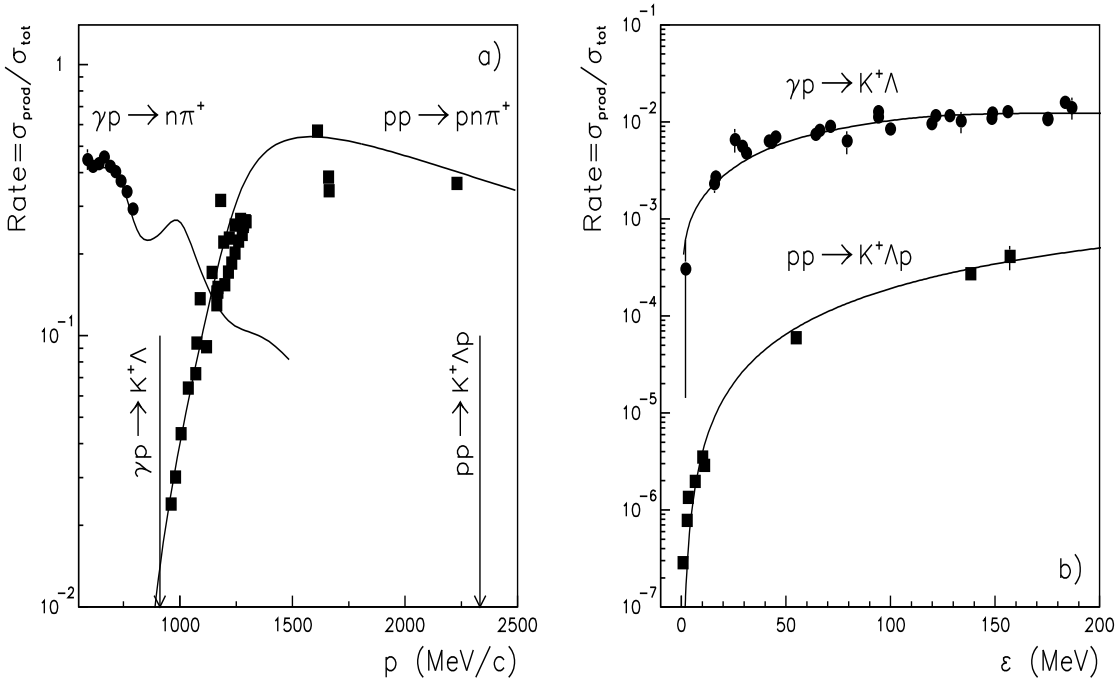

Figure 11. a) The rates of the $\gamma p \rightarrow n\pi^+$ and $pp \rightarrow pn\pi^+$ reactions as a function of the projectile momentum p. The arrow indicates the thresholds for the direct $\gamma p \rightarrow K^+\Lambda$ and $pp \rightarrow K^+\Lambda p$ production. b) The rates of the direct $\gamma p \rightarrow K^+\Lambda$ and $pp \rightarrow K^+\Lambda p$ production as a function of the excess energy ϵ. The data are from Ref. [18] while the lines show our calculations.

9. Conclusions

We have studied K^+-meson production in γC interactions at energies below the free $\gamma p \rightarrow K^+\Lambda X$ reaction threshold. The Thomas-Fermi and spectral function approximation were used in the calculation of the production process. It was found that these two models result in quite different total and differential cross sections for kaon photoproduction.

The difference between the two models for the target nucleon distribution can be detected in kaon photoproduction not only in the absolute scale, but also in the different shape of the spectra. The shapes of the transverse momentum spectra calculated with the two models seem to be identical at low transverse momenta p_t<170 MeV/c, but differ substantially at larger p_t. The large p_t region is sensitive to the details of the spectral function although the contribution from p_t>170 MeV/c to the total $\gamma C \rightarrow K^+ \Lambda X$ cross section is very small.

We have, furthermore, found that the contribution from secondary process $\gamma N \rightarrow \pi N$, $\pi N \rightarrow K^+ \Lambda$ to the kaon photoproduction is almost negligible for $E_\gamma \leq 1.2$ GeV. Therefore, the $\gamma C \rightarrow K^+ \Lambda X$ reaction qualifies as an optimal probe for an investigation of the in-medium nuclear dispersion relation.

The authors like to acknowledge discussions with T. Feuster and G. Penner.

REFERENCES

1. R.G. Newton, Scattering Theory of Waves and Particles, Springer-Verlag (1966)
2. A.K. Kerman, H. Mc. Manus and R.M. Thaler, Ann. Phys. 8 (1959) 55.
3. D.F. Jackson, Nuclear Reactions, Methuen (1970).
4. C. Ciofi degli Atti and S. Simula, Phys. Rev. C 53 (1996) 1689.
5. M.Q. Tran et al., Phys. Lett. B 445 (1998) 20.
6. C. Bennhold and L.E. Wright, Phys. Rev. C 39 (1989) 927.
7. A.S. Rosental et al., Ann. Phys. 184 (1988) 33.
8. C. Bennhold, Phys. Rev. C 39 (1989) 1944.
9. C. Bennhold, Nucl. Phys. A 547 (1992) 79c.
10. L.J. Abu-Raddal and J. Piekarewicz, nucl-th/9906066.
11. B. Zeidman et al., CEBAF Experiment 91-016.
12. C.E. Hyde-Wright, CEBAF Experiment 91-014.
13. M. Gourdin and J. Dufour, Il Nouvo Cim. 27 (1963) 1410.
14. H. Thom, Phys. Rev. 151 (1966) 1322.
15. Particle Data Group, Eur. Phys. J. A 3 (1998) 1.
16. T. Feuster and U. Mosel, Phys. Rev. C 58 (1998) 457.
17. T. Feuster and U. Mosel, Phys. Rev. C 59 (1999) 460.
18. Landolt-Börnstein, New Series 8 (1973) 285.
19. R. Williams, C.R. Ji and S.R. Cotanch, Phys. Rev. D 41 (1990) 1449.
20. F. James and M. Roos, Comp. Phys. Commun. 10 (1975) 343.
21. A. Sibirtsev and W. Cassing, Nucl. Phys. A 641 (1998) 476.
22. M. Hoffman et al., Nucl. Phys. A 593 (1995) 341.
23. K.S. Kölbig and B. Margolis, Nucl. Phys. B 6 (1968) 85
24. O. Benhar et al., Phys. Rev. Lett. 69 (1992) 1156
25. E. Vercellin et al., Il Nuovo Cim. A 106 (1993) 861
26. M. Effenberger and A. Sibirtsev, Nucl. Phys. A 632 (1998) 99.
27. C.W. Jager, C. Vries and H. Vries, At. Data Nucl. Data Tables 14 (1974) 480.
28. A. Sibirtsev, Sov. J. Nucl. Phys. 52 (1990) 295.
29. O. Benhar, A. Fabrocini and S. Fantoni, Nucl. Phys. A. 550 (1992) 201.

30. O. Benhar, A. Fabrocini and S. Fantoni, Nucl. Phys. A. 505 (1989) 201.
31. I. Sick et al., Phys. Lett. B 323 (1994) 267.
32. S. Frullani and J. Mougey, Adv. Nucl. Phys. 14 (1984) 1.
33. C. Gale, G. Bertsch and Das. Gupta, Phys. Rev. C 35 (1987) 1666.
34. G.M. Welke et al., Phys. Rev. C 38 (1988) 2101.
35. G.F. Bertsch, H. Kruse and S. Das Gupta, Phys. Rev. C 29 (1984) 673.
36. K. Weber et al., Nucl. Phys. A 552 (1993) 571.
37. E.D. Cooper, Phys. Rev. C 36 (1987) 2170.
38. S. Hama et al., Phys. Rev. C 41 (1990) 2737.
39. W. Greiner and J.A. Maruhn, Nuclear Models, Springer (1996).
40. R.B. Wiringa, Phys. Rev. C 38 (1988) 2967.
41. V.R. Pandharipande and S.C. Pieper, Phys. Rev. C 45 (1992) 791.
42. I. Sick, private communication.
43. S. Fantoni and V.R. Pandharipande, Nucl. Phys. A 427 (1984) 473.
44. C. Mahaux and R. Sartor, Nucl. Phys. A 546 (1992) 65.
45. M. Baldo et al., Nucl. Phys. A 545 (1992) 741.
46. C. Ciofi degli Atti, E. Pace and G. Salme, Phys. Rev. C 21 (1980) 805.
47. P.F. de Cordoba and E. Oset, Phys. Rev. C 46 (1992) 1697
48. A. Sibirtsev, W. Cassing and U. Mosel, Z. Phys. A 358 (1997) 357.
49. W. Cassing et al., Phys. Lett. B 238 (1990) 25.
50. A. Sibirtsev and M. Büscher, Z. Phys A 347 (1994) 191.
51. R.A. Arndt, I.I. Strakovsky and R.L. Workman, Phys. Rev. C 53 (1996) 430.
52. SAID Data Base, on-line facility.
53. K. Tsushima, S.W. Huang and A. Faessler, Phys. Lett. B 337 (1994) 245.
54. K. Tsushima, S.W. Huang and A. Faessler, J. Phys. G 21 (1995) 33.
55. M. Effenberger, A. Hombach, S. Teis and U. Mosel, Nucl. Phys. A 614 (1997) 501.